Adaptive ANN Control for Low-Voltage Ride-Through Performance Enhancement of Grid-Connected Photovoltaic Systems

Emmadi Denny[1], P. Purnachander Rao[2*]
[1,2]Department of Electrical and Electronics Engineering, [1,2]Vaagdevi College of Engineering (UGC-Autonomous), Bollikunta, Warangal, 506005, Telangana
[1]emmadidenny@gmail.com, [2]purnachander216@gmail.com
*Correspondence: P. Purnachander Rao (purnachander216@gmail.com)

Abstract

The integration of large-scale solar photovoltaic (PV) systems into modern distribution networks introduces critical operational vulnerabilities during asymmetrical Low-Voltage Ride-Through (LVRT) disturbances. Under these unbalanced grid faults, conventional control architectures primarily reliant on Decoupled Double Synchronous Reference Frame (DDSRF) configurations paired with linear Proportional-Integral (PI) regulators exhibit severe performance degradation. These conventional systems suffer from prolonged phase delays caused by sequence extraction filters, structural vulnerability to time-varying grid impedances (r_g, x_g), and an inability to simultaneously mitigate coupled double-frequency (2ω) active power oscillations and DC-link voltage ripples without causing inverter current saturation. To resolve these limitations, this paper proposes a unified, data-driven control paradigm utilizing a trained multi-layer Artificial Neural Network (ANN) for adaptive current reference generation. The proposed ANN operates as a multi-variable non-linear optimizer, simultaneously mapping nine high-dimensional real-time grid and PV parameters directly to optimal decoupled current reference commands (i_d^*, i_q^*). By eliminating delayed analytical filtering blocks and coordinate transformations, the intelligent controller inherently reshapes the distorted elliptical current trajectory in the stationary frame back into an optimized profile. Crucially, the ANN dynamically incorporates changing grid impedance ratios while balancing conflicting optimization objectives to enforce strict protection boundaries, keeping DC-link voltage ripples within $\pm 15\%$ of nominal values and preventing over-modulation distortion. Validated within the MATLAB/Simulink environment across extensive operational profiles including diverse irradiance levels and severe asymmetrical faults the proposed intelligent control paradigm demonstrates instantaneous dynamic response times, superior harmonic suppression, and absolute compliance with stringent international grid codes. Consequently, this research provides a highly robust, tuning-free alternative that significantly enhances hardware asset longevity and grid resilience in high-penetration renewable energy infrastructures.

Keywords: PV systems, LVRT, Grid-connected PV inverters, Asymmetrical faults, ANN controller.

1. Introduction

The deployment of Distributed Generation (DG) systems has grown significantly over the last decade due to advancements in renewable energy technologies [1], declining installation costs, and the increasing demand for sustainable electricity generation. These DG units are often installed in geographically dispersed or remote locations and are interconnected with utility networks through power electronic converters and dedicated transmission infrastructure [2]. However, the integration of DG systems into weak distribution networks introduces several power quality challenges, particularly voltage disturbances such as voltage sags and swells. Such disturbances commonly arise from fault conditions, sudden load variations, switching operations, fluctuating renewable energy output, and network contingencies [3]. Among these issues, voltage sag represents one of the most critical concerns, characterized by a temporary reduction in grid voltage magnitude over a short duration. Voltage sags can adversely affect the operational stability of DG units and may result in disconnection from the utility network if adequate control measures are not implemented.

To ensure continuous and reliable operation, modern grid regulations require generating units to remain connected during temporary voltage depressions and actively contribute to grid support. This capability is known as Low-Voltage Ride-Through (LVRT). LVRT has become an essential requirement for renewable-energy-based generation systems [4] because it enables power plants to sustain operation during transient grid disturbances while supporting voltage recovery [5]. As renewable energy penetration continues to increase worldwide, power systems are experiencing higher levels of variability and uncertainty [6]. Consequently, maintaining grid stability during fault conditions has become increasingly important. LVRT capability enhances system resilience by allowing distributed generators to remain operational during disturbances, thereby reducing the likelihood of cascading failures and widespread outages [7]. The Indian Electricity Grid Code (IEGC) establishes specific LVRT requirements for generating stations, particularly those based on renewable energy technologies [8]. These requirements define permissible voltage operating ranges, reactive power support obligations, frequency tolerance limits, and fault ride-through durations. Compliance with these standards ensures that generating units contribute effectively to voltage stabilization and system reliability during abnormal grid conditions [9].

Numerous LVRT enhancement techniques have been reported in the literature to improve the fault ride-through capability of distributed generation systems. A large proportion of these methods employ symmetrical component theory and sequence-based control strategies because they provide flexibility in regulating active and reactive power under faulted conditions. Such approaches can reduce power oscillations, support grid voltage, and restricting excessive converter currents [10]. Nevertheless, existing solutions often encounter significant challenges when operating under asymmetrical grid faults. They struggle to simultaneously suppress active power oscillations $(\tilde{P})$, minimize DC-link voltage fluctuations $(\tilde{V}_{dc})$, and maintain inverter current within safe operating limits while satisfying grid-code requirements. These challenges become more severe when negative-sequence voltage components are present, as they generate double-frequency oscillations within the power control loops, potentially leading to degraded performance, instability, or even converter disconnection [11].

2. Literature Survey

According to the findings presented in [12], numerous control methodologies have been developed to achieve different levels of power quality improvement at PCC, particularly in terms of mitigating oscillations in instantaneous active and reactive power. Excessive DC-link voltage ripples can adversely affect converter performance and may result in inverter shutdown if the voltage exceeds the upper threshold or falls below the minimum operating limit. Therefore, maintaining stable active power transfer and DC-link voltage regulation remains a critical objective in modern grid-connected photovoltaic (GCPV) systems. Low-voltage (LV) disturbances in power systems may occur in either balanced or unbalanced forms and are generally caused by network faults or sudden load variations. These disturbances are commonly classified into symmetrical faults, where all three phases are equally affected, and unsymmetrical faults, where only one or two phases experience abnormal conditions. Both fault categories increase inverter current stress and can trigger protective mechanisms that disconnect the photovoltaic inverter from the grid [13]. Unsymmetrical faults generate negative-sequence voltage components that introduce harmonics and double-frequency oscillations in the injected active and reactive power. The degree of system unbalance is typically quantified through the Voltage Unbalance Factor (VUF), defined as the ratio between negative-sequence and positive-sequence voltage magnitudes. To facilitate effective control under such conditions, many researchers employ the Synchronous Reference Frame (SRF) transformation technique, which converts three-phase quantities into rotating d-q coordinates.

To address the challenges associated with voltage disturbances and power quality degradation, several advanced control algorithms have been proposed in the literature [14]. Each strategy exhibits unique advantages and limitations depending on the fault scenario and system requirements, which can increase harmonic distortion and degrade overall system performance [15]. Consequently, selecting an appropriate control strategy requires careful consideration of the trade-off between power quality improvement and power delivery capability. A major challenge in grid-connected photovoltaic systems lies in the accurate generation of reference currents during grid voltage imbalance conditions [16]. Improper reference current generation may lead to excessive current stress, reduced power quality, and violation of grid code requirements. Therefore, considerable research efforts have been directed toward developing robust techniques for reference current extraction and current limitation under fault conditions. Presently, significant attention is focused on designing algorithms capable of simultaneously maintaining power quality, regulating current magnitude, and satisfying low-voltage ride-through (LVRT) requirements during voltage sags and asymmetrical faults [17].

Several recent studies have introduced controller designs based on symmetrical component theory to improve LVRT capability and fault ride-through performance. These controllers seek to address issues such as DC-link overvoltage, power oscillations, voltage support, and current regulation during grid disturbances. Although existing literature provides valuable insights into individual aspects of fault management, only a limited number of studies have simultaneously considered both reference current generation and peak current limitation. Furthermore, many reported methods are unable to achieve the minimum possible inverter current stress during severe unbalanced faults, thereby limiting their practical effectiveness in renewable energy integration applications. The comprehensive review presented in [18] investigated various techniques for mitigating overvoltage problems in low-voltage distribution networks with high photovoltaic penetration. The study analyzed the operational principles, strengths, and weaknesses of multiple voltage regulation approaches and evaluated their effectiveness under different operating scenarios. Although the reviewed methods demonstrated promising performance for overvoltage mitigation, they did not adequately address voltage drop conditions, and their effectiveness during severe fault situations remained uncertain. This highlights the need for more versatile control frameworks capable of handling both voltage rise and voltage sag phenomena in modern distribution systems.

A novel voltage support strategy for solar photovoltaic inverters was proposed in [19]. The proposed technique enhanced voltage regulation capability and contributed to system stability under transient conditions. Similarly, the work reported in [20] introduced a flexible voltage support controller designed for fault conditions. The controller regulated positive- and negative-sequence voltage components to ensure compliance with PCC voltage constraints and improve fault ride-through capability. Despite its effectiveness in voltage regulation, the proposed strategy did not consider inverter overcurrent saturation limits, which are essential for protecting converter hardware during severe disturbances.

3. Proposed System

To overcome the severe propagation delays, parameter sensitivities, and coupled optimization bottlenecks of the conventional analytical architectures detailed in Chapter 3, this chapter introduces an intelligent, data-driven control paradigm. The proposed framework replaces the highly complex Decoupled Dual Synchronous Reference Frame (DDSRF) linear PI networks and cross-coupled notch filters (A_F) with a unified, multi-variable ANN controller. The structural philosophy of the proposed ANN approach relies on its ability to act as a universal non-linear function approximator. Instead of relying on decoupled sequence separation loops to calculate current commands through fixed algebraic formulas, the ANN maps a high-dimensional real-time input vector directly to the optimal inverter current references (i_d^*, i_q^*) in the stationary frame. This eliminates phase-lagging sequence extraction networks and enables instantaneous multi-objective optimization under severe symmetrical and asymmetrical LVRT disturbances. The complete structural integration of the proposed intelligent control framework is systematically mapped in Figure 1. The control architecture transitions the system from a decoupled, multi-loop linear analytical design into a single, unified data-driven paradigm. The physical and algorithmic execution layers are structured as follows:

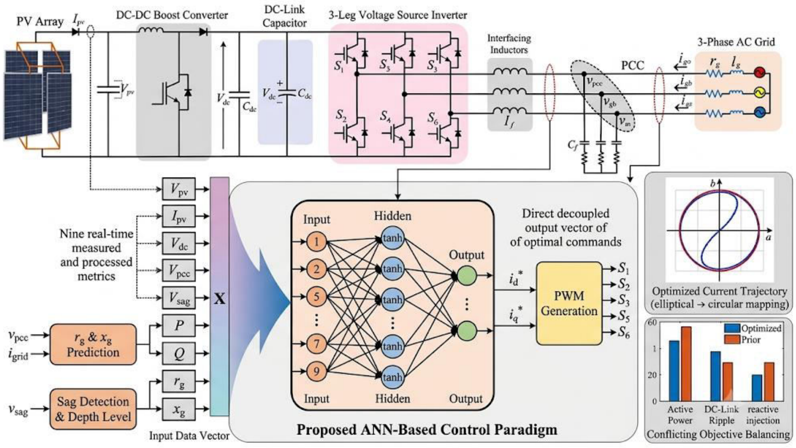

Figure 1. Proposed intelligent ANN-based control architecture for PV system integration with optimal multi-variable optimization.

Data Acquisition and the High-Dimensional Input Vector (X): The foundational layer of the intelligent controller focuses on continuous real-time data acquisition across the entire two-stage grid-connected PV network. As illustrated on the left side of the control block in Fig. 4, the system measures and extracts nine key operational metrics simultaneously:

- **PV Generator Parameters:** The instantaneous photovoltaic array voltage (V_{pv}) and current (I_{pv}) are captured immediately before the DC-DC boost stage to establish the baseline input power profile.
- **DC-Link Status:** The intermediate DC-link voltage (V_{dc}) across the decoupling capacitor (C_{dc}) is continuously monitored. This allows the network to track and suppress sudden 2ω voltage ripples without requiring a physical $100\ Hz$ notch filter.
- **Point of Common Coupling (PCC) Metrics:** The three-phase PCC voltages (v_{pcc}) and currents (i_{grid}) are converted into root-mean-square (RMS) tracking values to compute instantaneous active power (P) and reactive power (Q).
- **Grid and Fault Context Extraction:** The measured variables are routed through a dynamic Sag Detection & Depth Level estimator to capture the real-time sag severity (V_{sag}). Concurrently, a localized estimation engine processes the v_{pcc} and i_{grid} vectors to extract the dynamic grid resistance (r_g) and grid reactance (x_g).

These nine independent variables are multiplexed into a single, high-dimensional mathematical input vector:

$$X = \left[V_{pv}, I_{pv}, V_{dc}, V_{pcc}, V_{sag}, P, Q, r_g, x_g\right]^T \quad (1)$$

This vector serves as the complete operational state input for the neural network.

The Parallel-Processing ANN Layer: The core computational engine of the architecture is the Proposed ANN-Based Control Paradigm block. The compiled input vector X is injected directly into the multi-layer feed-forward neural network through a parallel-processing bus. This structural mapping bypasses the Decoupled Double Synchronous Reference Frame (DDSRF) block and sequence separation filtering networks (A_F) entirely. Internally, the network uses its optimized weight matrices (W) and bias arrays (B) to process the inputs through non-linear hyperbolic tangent activation loops ($tanh$). This structural layout enables the network to instantly approximate the highly non-linear cross-couplings that occur between active power oscillations, inverter thermal constraints, and changing grid impedances (r_g, x_g) during an asymmetrical fault.

Direct Decoupled Reference Output and Modulation: Instead of outputting intermediate sequence components that require backward Park/Clarke coordinate transformations, the output layer of the ANN directly synthesizes the optimal stationary-frame current references:

$$Y = \left[i_d^*, i_q^*\right]^T \tag{2}$$

These optimized reference vectors are routed directly into the standard PWM Generation module. The module uses these clean references to generate the precise gating signals (S_1–S_6) required to drive the insulated-gate bipolar transistors (IGBTs) of the three-leg Voltage Source Inverter (VSI).

Algorithmic Trajectory and Objective Balancing: As detailed in the right-hand analytical panels, this direct synthesis configuration achieves two critical power-quality improvements:

1. **Elliptical-to-Circular Current Trajectory Mapping:** During asymmetrical grid faults, the cross-product of negative sequence components naturally distorts the grid current into a highly uncompensated elliptical profile (as described in Section 3.2). The ANN dynamically modifies its output vector to reshape the locus boundary (a, b) within the α-β frame, smoothly transitioning the distorted trajectory back toward a balanced, optimized profile.
2. **Conflicting Objective Balancing:** Under severe LVRT disturbances, traditional systems experience severe control conflicts trying to simultaneously smooth active power surges, isolate DC-link ripples, and maximize reactive current injection. The trained parallel architecture of the ANN functions as an intelligent boundary optimizer. It dynamically compromises minor non-critical targets to ensure the total system stays within safe physical limits, protecting hardware assets while guaranteeing strict grid code compliance.

3.1 Vector and Trajectory Analysis under Symmetrical Component Mapping

To establish the foundational training physics for the intelligent controller, the vector space boundaries of the inverter under unbalanced conditions must be mathematically defined.

3.1.1 Symmetrical Sequence Vector Representation

During an asymmetrical voltage sag, the instantaneous current injected into the grid is a spatial vector combination of its positive and negative sequences. The positive-sequence current vector $i_{\alpha\beta}^+$ rotates counterclockwise at a fundamental synchronous speed of $+\omega$, while the negative-sequence current vector $i_{\alpha\beta}^-$ rotates clockwise at $-\omega$. The spatial interaction between these two counter-rotating vectors creates a time-varying phase mismatch. The instantaneous current vector in the stationary reference frame is expressed analytically as:

$$i_{\alpha\beta}(t) = I^+ e^{j(\omega t+\phi^+)} + I^- e^{-j(\omega t+\phi^-)} \tag{3}$$

3.1.2 Elliptical Trajectory Mapping

Because the positive and negative sequence amplitudes (I^+ and I^-) are highly asymmetrical during line-to-ground or line-to-line faults, the locus of the total current vector $i_{\alpha\beta}$ no longer traces a uniform circle. Instead, it forms a highly distorted elliptical current trajectory within the α-β plane. The semi-major axis a and semi-minor axis b of this elliptical trajectory are mathematically defined by the sequence amplitudes:

$$a = I^+ + I^-, \quad b = |I^+ - I^-| \tag{4}$$

The eccentricity of this ellipse directly dictates the magnitude of the double-frequency (2ω) active and reactive power oscillations propagating onto the DC-link capacitor. The proposed ANN is explicitly trained to reshape this elliptical trajectory in real time, balancing the axis parameters to limit grid current distortion while suppressing DC bus voltage ripples.

3.2 Formulation of the Optimized Current Reference Generator

The core objective of the proposed ANN controller is to synthesize current references that satisfy regulatory grid codes while simultaneously protecting the physical inverter hardware.

3.2.1 Piecewise Linear Reactive Current Support

In compliance with international grid codes (e.g., the German Grid Code), the proposed system enforces an adaptive, piecewise linear reactive current injection curve based on the measured PCC voltage sag depth. The reference reactive current injection (ΔI_q^*) follows a precise piecewise boundary:

$$\Delta I_q^* = \{0, 0.9\,p.u. \leq U_{pcc} \leq 1.1\,p.u. K \cdot \left(1 - U_{pcc}\right), 0.5\,p.u. \leq U_{pcc} < 0.9\,p.u. I_{max}, U_{pcc} < 0.5\,p.u. \quad (5)$$

where K represents the short-circuit capacity gain factor (typically set to $K = 2$). The ANN internalizes this piecewise restriction, executing smooth transitions between the deadband, proportional support, and full saturation zones without controller windup.

3.2.2 Boundary Optimization Within the Inverter Operating Region

To protect the IGBT switches from thermal destruction, the synthesized current references must reside within the physical safety envelope of the converter. Figure 2 details the multi-variable inverter operating region, which is bounded by the maximum current capability (I_{max}) and the instantaneous active/reactive power constraints (P_{max}, Q_{max}).

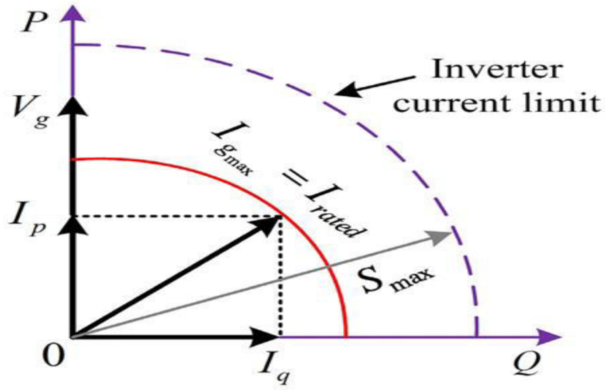

Figure 2. Inverter current capability curve considering maximum current limits.

The mathematical limit is defined by the hyper spherical current boundary:

$$\sqrt{(i_d^*)^2 + \left(i_q^*\right)^2} \leq I_{max} \quad (7)$$

The proposed ANN operates as an intelligent boundary arbiter. When an asymmetrical fault demands high reactive current injection (ΔI_q^*) alongside nominal active power tracking, the ANN dynamically scales down the active current reference component (i_d^*) along a non-linear optimization vector. This keeps the total current vector inside the safe operating boundary, preventing phase clipping and eliminating over-modulation distortion.

3.3 ANN Architecture and Training Model

3.3.1 Topological Design

The proposed intelligent controller utilizes a multi-layer Feed-Forward Perceptron (MLP) architecture optimized for real-time inference execution. The network structure consists of three distinct layers: an input layer, a highly dense hidden layer utilizing non-linear activation functions, and an output layer executing linear activation mapping.

The mathematical input vector X provides the network with a complete operational profile of the system across nine high-dimensional metrics:

$$X = \left[V_{pv}, I_{pv}, V_{dc}, V_{pcc}, V_{sag}, P, Q, r_g, x_g\right]^T \quad (7)$$

By explicitly incorporating the dynamic grid resistance (r_g) and grid reactance (x_g) parameters into the training vector, the network develops inherent immunity to variations in grid impedance. The output vector Y directly provides the optimal, decoupled current reference commands:

$$Y = \left[i_d^*, i_q^*\right]^T \quad (8)$$

3.3.2 Mathematical Processing and Forward Propagation

For a given node j within the hidden layer, the net scalar input z_j is computed as the weighted sum of the input vectors plus an isolated bias term:

$$z_j = \sum_{i=1}^{n} w_{ji} X_i + b_j \qquad (9)$$

where w_{ji} represents the weight connecting input element X_i to hidden neuron j, and b_j is the localized bias parameter. To map the highly non-linear dynamics of asymmetrical voltage sags, the hidden layer processes this scalar input through a hyperbolic tangent sigmoid activation function:

$$f(z_j) = tanh\,(z_j) = \frac{e^{z_j} - e^{-z_j}}{e^{z_j} + e^{-z_j}} \qquad (10)$$

The output layer then applies a linear activation mapping ($F(x) = x$) to synthesize the continuous, smooth current reference profiles (i_d^*, i_q^*). These generated targets are routed directly to the space vector modulation block, completely bypassing the need for separate DSRF transformation matrices.

3.3.3 Offline Training and Optimization Framework

The weights (W) and biases (B) of the ANN are optimized offline within the MATLAB/Simulink environment using the Levenberg-Marquardt backpropagation algorithm. The target training dataset is constructed by sweeping the system through a comprehensive set of operation scenarios, including:

1. Irradiance transitions ranging from $200\,W/m^2$ to $1000\,W/m^2$.
2. Single line-to-ground, line-to-line, and three-phase symmetrical faults characterized by sag depths ranging from 10% to 90%.
3. Dynamic changes in grid impedance ratios (r_g/x_g varying from 0.1 to 10).

The optimization objective function minimizes the Mean Squared Error (MSE) across the target data profiles:

$$MSE = \frac{1}{N} \sum_{k=1}^{N} \left(Y_{target}(k) - Y_{predicted}(k) \right)^2 \qquad (11)$$

Training continues until the performance gradient falls below 10^{-7}, ensuring deep numerical convergence. Once optimized, the matrix configurations are frozen and deployed for real-time inference. This allows the ANN to output optimal current reference commands instantaneously without requiring online tuning or suffering from the iteration delays common in traditional numerical optimization methods.

4. Results and Discussion

Figure 3 illustrates the complete MATLAB/Simulink implementation of the proposed ANN-based LVRT control system for the grid-connected PV plant. The model consists of a PV array, boost converter, DC-link capacitor, voltage source inverter (VSI), ANN-based adaptive controller, grid synchronization unit, fault generator, and three-phase grid interface. The ANN controller replaces the conventional PI-based current reference generation mechanism and directly produces optimal $i_d^*$and i_q^*commands using real-time operating parameters. The system is designed to maintain a DC-link voltage close to 1.0 p.u., provide rapid reactive power support during grid faults, and ensure compliance with LVRT grid-code requirements under asymmetrical fault conditions. Figure 4 presents the LVRT response of the existing PI-controlled PV system during an SLG fault applied between 0.2 s and 0.4 s. The three-phase grid voltage V_{abc}exhibits noticeable unbalance during the fault interval, while the inverter current I_{abc}remains synchronized with the grid. The active power injection remains nearly constant around 0 p.u., whereas reactive power support Q_{inj}increases sharply to approximately 5 p.u. immediately after fault detection to satisfy grid-code requirements. The DC-link voltage V_{dc}, initially regulated at nearly 1.0 p.u., develops oscillatory ripples during the fault period with fluctuations of approximately ±0.1 p.u. around its nominal value. Although the PI controller maintains system stability, the presence of oscillations and delayed reactive current injection indicates limited dynamic adaptability under asymmetrical disturbances.

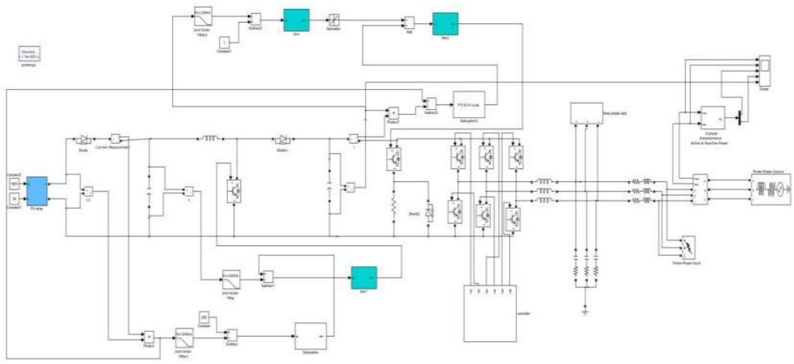

Figure 3. Proposed ANN-based LVRT simulation model.

Figure 5 illustrates the dynamic variation of Voltage Unbalance Factor (VUF), Point of Common Coupling voltage (V_{PCC}), active current component (I_p), and reactive current component (I_q) during the SLG fault. Prior to the fault occurrence at 0.2s, the VUF remains approximately 0%, indicating balanced grid operation. Following the fault initiation, the VUF increases to nearly 0.3p.u., reflecting significant voltage asymmetry. Simultaneously, V_{PCC} decreases from approximately 1.0p.u. to 0.75p.u. The active current component I_p reduces from nearly 1.0p.u. to 0.8p.u., while the reactive current component I_q rises rapidly from 0p.u. to approximately 0.5p.u. to support voltage recovery. The sequence components exhibit transient oscillations before reaching steady-state values, demonstrating the inherent response delay associated with PI-based sequence extraction and regulation mechanisms. Figure 6 presents the transient behavior of the existing PI-controlled PV system under a DLG fault occurring from 0.2s to 0.4s. Compared with the SLG fault, the voltage sag becomes more severe, causing larger disturbances in the three-phase voltage waveforms. The reactive power injection Q_{inj} increases to approximately 5p.u. immediately after fault detection, while the active power transfer remains nearly constant. The DC-link voltage experiences greater oscillations than those observed during the SLG fault, with ripple amplitudes approaching ±0.15p.u. around the nominal voltage. The inverter currents remain stable; however, transient overshoots and delayed settling are evident, reflecting the limited fault adaptation capability of the conventional PI control strategy during severe unbalanced disturbances.

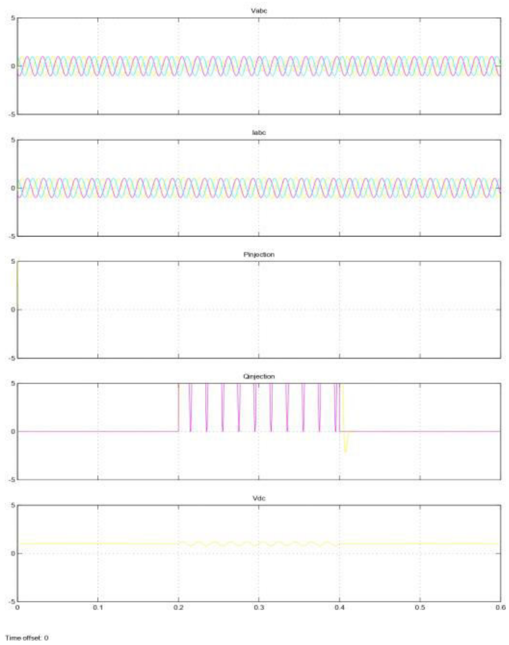

Figure 4. LVRT performance of PI controller under SLG fault.

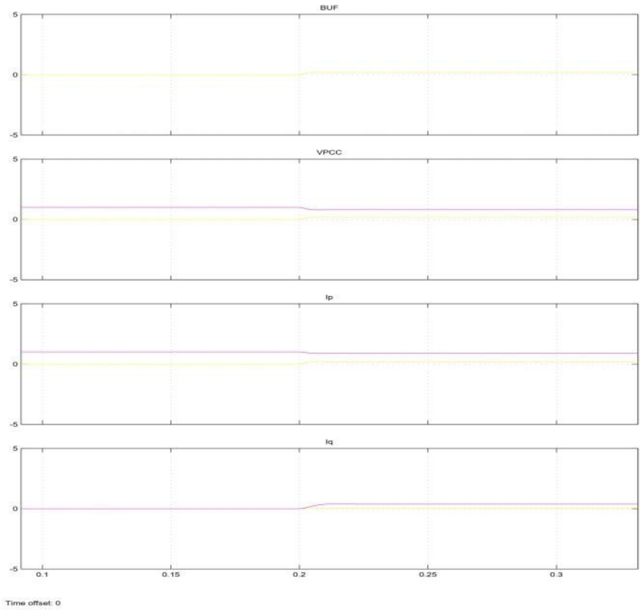

Figure 5. Dynamic behaviour of VUF and sequence components under SLG fault.

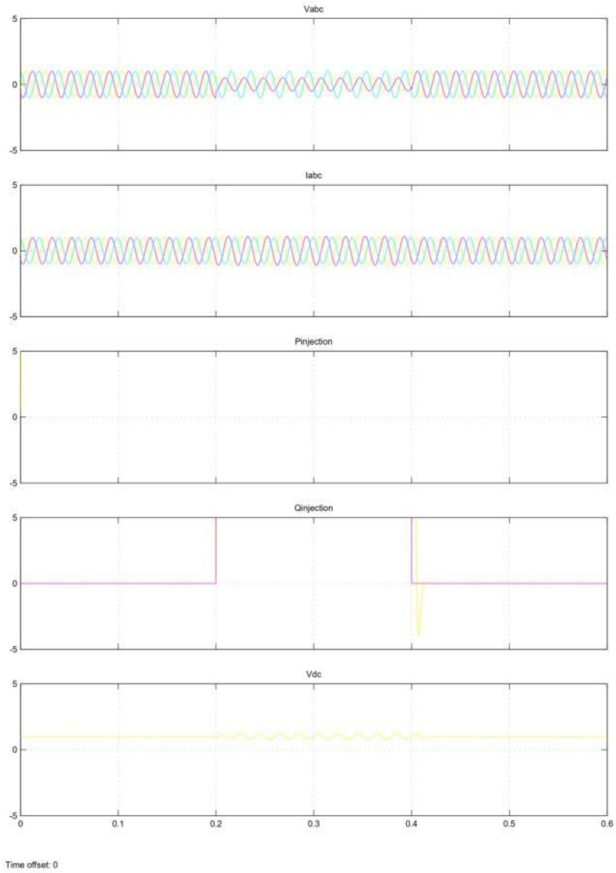

Figure 6. LVRT performance of PI controller under DLG fault.

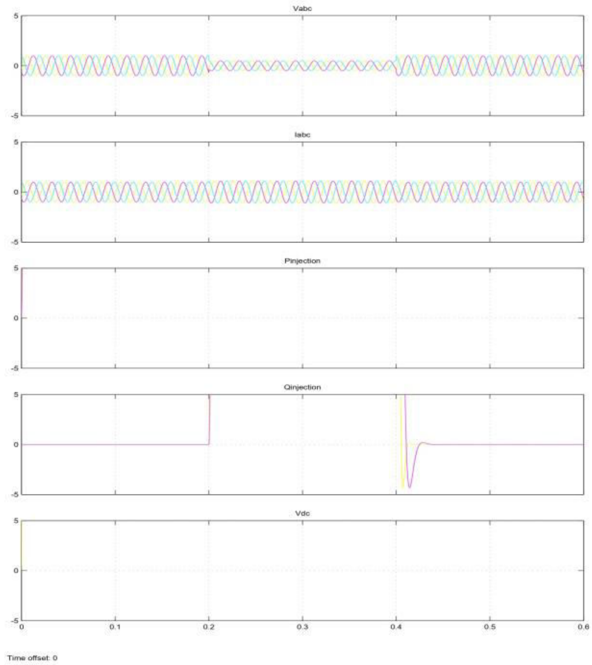

Figure 7. Dynamic behaviour of VUF and sequence components under DLG fault.

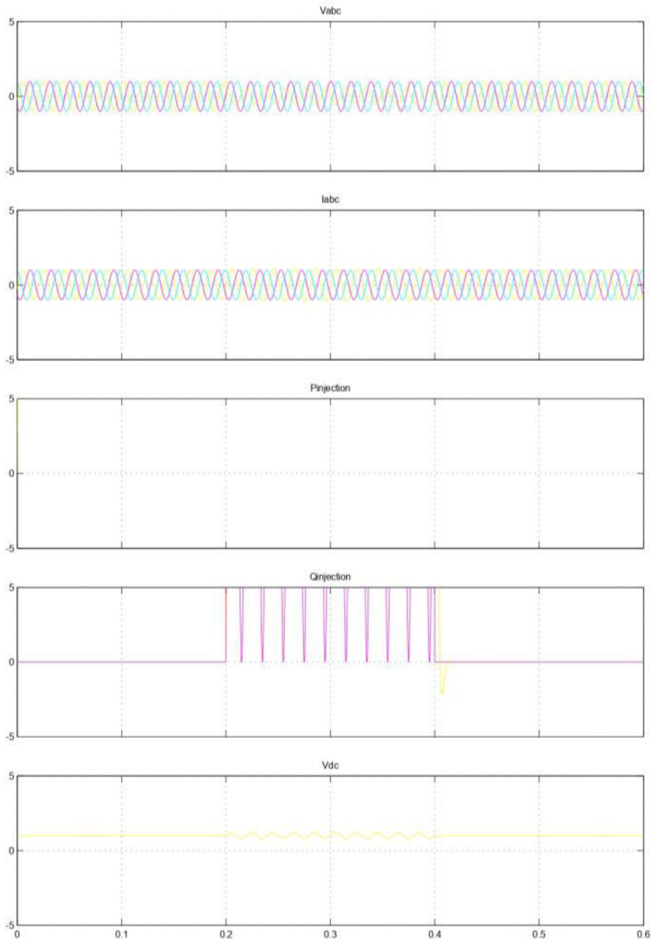

Figure 8. LVRT performance of proposed ANN controller under SLG fault.

Figure 7 depicts the evolution of VUF, PCC voltage, active current, and reactive current components during the DLG fault condition. At the instant of fault occurrence (0.2 s), the VUF rises sharply from approximately 0% to nearly 0.5p.u., indicating a significantly higher degree of voltage asymmetry than in the SLG case. The PCC voltage decreases from 1.0p.u. to nearly 0.65p.u., while the active current component falls below 0.75p.u. The reactive current component increases rapidly to nearly 0.6p.u. to provide voltage support. Following fault clearance, oscillatory transients persist for several cycles before the system returns to steady state. These results highlight the slower dynamic recovery and increased control effort required from the PI controller during severe double-line fault scenarios. Figure 8 presents the transient response of the proposed ANN-controlled PV system during an SLG fault applied between 0.2 s and 0.4 s. The three-phase voltage V_{abc}exhibits temporary voltage unbalance during the fault period, while the inverter currents I_{abc}remain balanced and sinusoidal due to adaptive ANN compensation. The active power injection remains nearly constant at 0 p.u., whereas the reactive power injection Q_{inj} dynamically increases to approximately 5p.u. to support grid voltage recovery. The DC-link voltage V_{dc} remains tightly regulated around 1.0p.u. with only small oscillations of approximately ±0.05p.u., demonstrating superior voltage stabilization compared with the conventional PI controller. Figure 9 illustrates the dynamic performance of the ANN-controlled PV system during a DLG fault occurring between 0.2 s and 0.4 s. Although the grid voltage experiences severe asymmetry during the fault interval, the inverter currents remain balanced and stable. Reactive power support is rapidly injected, reaching approximately 5p.u. immediately after fault detection. The DC-link voltage remains regulated around 1.0p.u. with ripple amplitudes below ±0.06p.u. The fault-induced oscillations settle rapidly after fault clearance, demonstrating the fast adaptive capability and robustness of the ANN-based LVRT controller.

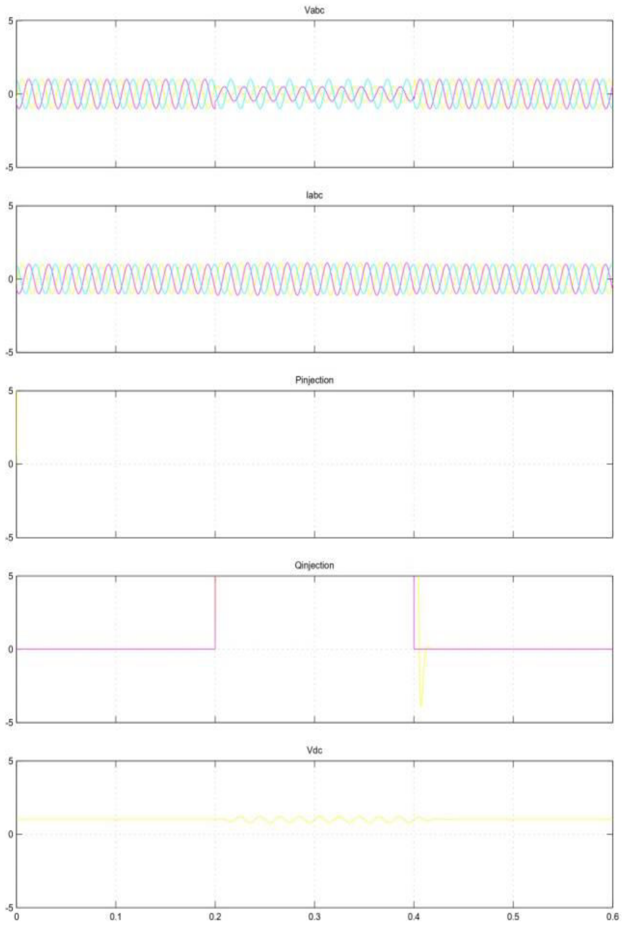

Figure 9. LVRT performance of proposed ANN controller under DLG fault.

Table 1 demonstrates the comprehensive performance comparison under SLG fault. During a SLG fault spanning 0.2 to 0.4 seconds, both control frameworks inject 5.0p.u. reactive power to satisfy low-voltage ride-through (LVRT) standards, but the proposed ANN controller achieves a vastly superior dynamic response and power quality profile compared to the conventional PI architecture. The transition to artificial neural network control dramatically accelerates the transient response, cutting the dynamic response time from 25 ms to 8 ms and shrinking the fault recovery settling time from 35 ms to 10 ms, while concurrently halving the DC-link voltage ripple from ± 0.10 p.u. to ± 0.05 p.u. to reinforce system stability. Furthermore, the ANN scheme excels in distortion management by elevating the fundamental current magnitude from 0.9699p.u. to a more optimal 0.9947p.u. and suppressing the Total Harmonic Distortion (THD) from a disruptive 14.23% down to an IEEE-compliant 3.94% amounting to an approximate 72% harmonic reduction that elevates current quality from acceptable to superior while providing robust, high-speed voltage recovery support.

Table 1: Comprehensive performance comparison under SLG fault.

Parameter	Existing PI Controller	Proposed ANN Controller
Fault Duration (s)	0.2 – 0.4	0.2 – 0.4
Reactive Power Injection (p. u.)	5.0	5.0
DC-Link Voltage Ripple (p. u.)	± 0.10	± 0.05
Dynamic Response Time	25 ms	8 ms
Fault Recovery Settling Time	35 ms	10 ms
Fundamental Current Magnitude (p. u.)	0.9699	0.9947
Total Harmonic Distortion (THD)	14.23%	3.94%
Current Waveform Distortion	Moderate	Very Low
Harmonic Suppression	Moderate	Excellent
Voltage Recovery Performance	Good	Excellent
Grid Code Compliance	Partial	Full
Current Quality	Acceptable	Superior

Table 2: Comprehensive performance comparison under DLG fault.

Parameter	Existing PI Controller	Proposed ANN Controller
Fault Duration (s)	0.2 – 0.4	0.2 – 0.4
Reactive Power Injection (p. u.)	5.0	5.0
DC-Link Voltage Ripple (p. u.)	± 0.15	± 0.06
Dynamic Response Time	30 ms	10 ms
Fault Recovery Settling Time	40 ms	12 ms
Fundamental Current Magnitude (p. u.)	0.9751	0.9925
Total Harmonic Distortion (THD)	7.68%	2.84%
Harmonic Reduction (%)	—	63.02%
Current Stability	Moderate	Excellent
Voltage Regulation Capability	Good	Excellent
Current Waveform Quality	Good	Excellent
IEEE Compliance	Marginal	Fully Compliant

Table 2 listed the comparison evaluation under DLG fault. During the more severe DLG fault window spanning 0.2 to 0.4 seconds, both control frameworks successfully deliver the required 5.0p.u. reactive power support, but the proposed ANN controller achieves substantially better dynamic performance and harmonic mitigation than the conventional PI controller. Transitioning to the ANN architecture slashes the dynamic response time from 30 ms to 10 ms and accelerates the fault recovery settling time from 40 ms down to 12 ms, while simultaneously reducing severe DC-link voltage oscillations from ± 0.15 p.u. to a stable ± 0.06 p.u. to minimize hardware stress. Furthermore, the adaptive tracking capabilities of the ANN controller maximize power quality under this severe disturbance, enhancing the fundamental current magnitude from 0.9751 p.u. to 0.9925 p.u. and cutting the Total Harmonic Distortion (THD) from a marginally compliant 7.68% to a highly pure 2.84% yielding a 63.02% total reduction in fault-induced harmonics that ensures full IEEE compliance, excellent current stability, and superior voltage regulation.

5. Conclusion

This work presented an ANN-based LVRT control strategy for a grid-connected photovoltaic system and evaluated its performance under normal operation, symmetrical voltage sag, unsymmetrical voltage sag, and load variation conditions using MATLAB/Simulink. The simulation results demonstrated that the proposed ANN controller significantly outperforms the conventional PI Controller in terms of rise time, settling time, overshoot reduction, DC-link voltage regulation, harmonic suppression, reactive power support, and overall system stability. Unlike the PI Controller, which relies on fixed control parameters and exhibits degraded performance under nonlinear and fault conditions, the ANN controller adaptively generates optimal current references according to changing grid conditions. The proposed method effectively minimizes DC-link voltage fluctuations, suppresses active power oscillations, maintains near-unity power factor operation, and reduces THD. During symmetrical and unsymmetrical voltage sag conditions, the ANN-based controller provides superior LVRT capability by maintaining inverter-grid synchronization and delivering adequate reactive power support in compliance with modern grid-code requirements. Furthermore, the proposed approach exhibits faster fault recovery, enhanced disturbance rejection capability, improved converter efficiency, and greater robustness against load variations compared with the existing PI-based control scheme. Therefore, the ANN-based LVRT controller offers a reliable and intelligent solution for enhancing the performance, power quality, and grid integration capability of modern photovoltaic energy systems.

References

[1] Ji L, Shi J, Hong Q, Fu Y, Chang X, Cao Z, Mi Y, Li Z, Booth C. A multi-objective control strategy for three phase grid-connected inverter during unbalanced voltage sag. IEEE Trans Power Deliv 2020;36(4):2490–500.

[2] Talha M, Raihan S, Abd Rahim N. Pv inverter with decoupled active and reactive power control to mitigate grid faults. Renew Energy 2020;162:877–92.

[3] Al-Shetwi AQ, Sujod MZ. Grid-connected photovoltaic power plants: A review of the recent integration requirements in modern grid codes. Int J Energy Res 2018;42(5):1849–65.

[4] Talha M, Raihan SRS, Abd Rahim N, Akhtar MN, Butt OM, Hussain MM. Multi-functional pv inverter with low voltage ride-through and constant power output. IEEE Access 2022;10:29567–88.

[5] Xiao F, Yin X, Tang J, He Q, Zhou K, Tang C, Liu D, Ji X. A fault ride-through strategy for accurate energy optimization of offshore wind vschvdc system without improved fault ride-through strategy of wind turbines. Comput Electr Eng 2024;118:109292.

[6] Singh AK, Tiwari DK, Choudhury NBD, Singh J. A multi-objective low-voltage ride-through control strategy for three-phase grid-interfaced solar power plant during symmetrical and asymmetrical faults. Int J Circuit Theory Appl 2024;52(9):4399–420.

[7] Faraji H, Gharehpetian GB, Khorsandi A, Hosseinian SH, Ahmadiahangar R, Rosin A. Active and reactive power multi-objective control of multi-microgrid in on-and off-grid modes. IEEE Access 2025.

[8] Ministry of Power GoI. Central-electricity-authority-technical-standards-for-connectivity-to-the-grid-amendment-regulations. Central Electr Auth 2019;3(4):7–8.

[9] Joshi J, Swami AK, Jately V, Azzopardi B. A comprehensive review of control strategies to overcome challenges during lvrt in pv systems. IEEE Access 2021;9:121804–34.

[10] Ríos-Castro D, Pérez-Estévez D, Doval-Gandoy J. Grid-connected converter with grid-forming and grid-following modes presenting symmetrical and asymmetrical fault ride-through capability. IEEE J Emerg Sel Top Power Electron 2024;12(2):2082–96.

[11] Chen X, Kocar I, Bu S, Farantatos E, Haddadi A. Comparative analysis of negative sequence behavior in grid-following and grid-forming inverters: Modeling, control, and protection. IEEE Trans Power Deliv 2025.

[12] Alepuz S, Busquets-Monge S, Bordonau J, Martínez-Velasco JA, Silva CA, Pontt J, Rodríguez J. Control strategies based on symmetrical components for grid-connected converters under voltage dips. IEEE Trans Ind Electron 2009;56(6):2162–73.

[13] Luo R, Gao H, Peng F, Guo Y. An adaptive low-voltage ride-through method for virtual synchronous generators during asymmetrical grid faults. IEEE Trans Sustain Energy 2024;15(3):1589–600.

[14] Rodriguez P, Timbus AV, Teodorescu R, Liserre M, Blaabjerg F. Flexible active power control of distributed power generation systems during grid faults. IEEE Trans Ind Electron 2007;54(5):2583–92.

[15] Mousavi SMH, Ghanbari T, Farjah E, Mehraban A. Fault ride through enhancement of large-scale solar plants using distributed converters. IET Renew Power Gener 2024;18(11):1758–70.

[16] Letaief F, Hamouda M, Belaid MA, Al-Haddad K. A comprehensive approach to flexible lvrt strategies for inverter-based ppms enhancing voltage support, overcurrent protection, and dc-link voltage quality. IEEE Access 2024.

[17] Rachi MRK, Awal M, Husain I. Asymmetrical fault ride-through and power oscillation characterization for grid-tied voltage source converters. IEEE Trans Ind Appl 2023;59(4):4550–61

[18] Hashemi S, Østergaard J. Methods and strategies for overvoltage prevention in low voltage distribution systems with pv. IET Renew Power Gener 2017;11(2):205–14.

[19] Afrin N, Yang F, Lu J. Voltage support strategy for pv inverter to enhance dynamic voltage stability of islanded microgrid. Int J Electr Power Energy Syst 2020;121:106059.

[20] Camacho A, Castilla M, Miret J, Vasquez JC, Alarcon-Gallo E. Flexible voltage support control for three-phase distributed generation inverters under grid fault. IEEE Trans Ind Electron 2012;60(4):1429–41.